

A Self-Powered Angle Sensor at Nanoradian-Resolution for Robotic Arms and Personalized Medicare

Ziming Wang, Jie An, Jinhui Nie, Jianjun Luo, Jiajia Shao, Tao Jiang, Baodong Chen, Wei Tang,* and Zhong Lin Wang*

As the dominant component for precise motion measurement, angle sensors play a vital role in robotics, machine control, and personalized rehabilitation. Various forms of angle sensors have been developed and optimized over the past decades, but none of them would function without an electric power. Here, a highly sensitive triboelectric self-powered angle sensor (SPAS) exhibiting the highest resolution (2.03 nano-radian) after a comprehensive optimization is reported. In addition, the SPAS holds merits of light weight and thin thickness, which enables its extensive integrated applications with minimized energy consumption: a palletizing robotic arm equipped with the SPAS can precisely reproduce traditional Chinese calligraphy via angular data it collects. In addition, the SPAS can be assembled in a medicare brace to record the flexion/extension of joints, which may benefit personalized orthopedic recuperation. The SPAS paves a new approach for applications in the emerging fields of robotics, sensing, personalized medicare, and artificial intelligence.

With the rapid advance in robot-related technologies, robots have become more intelligent, miniaturized and ubiquitous in our daily life.^[1] Except conveniences provided, several major unsolved challenges have been posed.^[2] Among them, angle measurement is vitally important since it has been widely applied in robotics, medicare, industrial control and even artificial intelligence.^[3] Impressive progress has been achieved on

angle measurement over past decades, these breakthroughs mainly focus on developing sensors based on operating mechanisms including optoelectrical effect, electromagnetic effect and an inertial measurement unit (IMU).^[4] However, additional electric power is required for driving these sensors, and none of them would work without power, which is unsatisfactory for situations suffered from limited energy supply. On the other hand, connections between the Internet of Things (IoT) and human beings are getting increasingly diverse at an accelerating pace due to the IoT could link physical devices with each other via collecting and communicating data.^[5] Hence, numerous sensors will be fabricated and installed on these appliances to constitute the supporting infrastructure which costs huge additional energy consumption and

usually more than the local IoT devices do.^[6] In addition to developing more efficient strategies for energy storage and conversion, fabricating self-powered sensors is an alternative and also effective strategy to cope with these practical challenges arose from both the advance in robotics and the advent of the era of IoT.^[7]

The underlying technology dictates the operating mechanism of a sensor and its response characteristics to external stimuli. The triboelectric nanogenerator (TENG) technology originates from Maxwell's displacement current and roots in the coupling of the triboelectrification effect as well as the electrostatic induction.^[8] It has demonstrated advantages of converting external mechanical agitations into electric signals with rather high magnitude in a straightforward way.^[9] Additionally, the triboelectric effect is ubiquitous and ascribed to contact between two different interfaces, which not only ensures the conversion of miscellaneous mechanical stimuli into high-magnitude signals but also enables broad materials choices for us.^[10] Therefore, TENG technology has been extensively utilized in micro/nano-power source,^[11] blue energy,^[12] and self-powered sensors.^[13] Several attempts to develop self-powered angle sensor have been reported as follows: Xu et al. devised a triboelectric angle sensor based on hydrogel, nonetheless, this device can only generate qualitatively signals indicating the movement of joints;^[14] Wu et al. designed a highly reliable self-powered angle sensor based on the principle of encoder. However, complicated pattern on the top electrode has to be

Dr. Z. Wang, Dr. J. An, Dr. J. Nie, Dr. J. Luo, Dr. J. Shao, Prof. T. Jiang, Prof. B. Chen, Prof. W. Tang, Prof. Z. L. Wang
CAS Center for Excellence in Nanoscience
Beijing Key Laboratory of Micro-nano Energy and Sensor
Beijing Institute of Nanoenergy and Nanosystems
Chinese Academy of Sciences
Beijing 100083, P. R. China
E-mail: tangwei@binn.cas.cn; zhong.wang@mse.gatech.edu

Dr. Z. Wang, Dr. J. An, Dr. J. Nie, Dr. J. Luo, Dr. J. Shao, Prof. T. Jiang, Prof. B. Chen, Prof. W. Tang, Prof. Z. L. Wang
School of Nanoscience and Technology
University of Chinese Academy of Sciences
Beijing 100049, P. R. China
Prof. Z. L. Wang
School of Material Science and Engineering
Georgia Institute of Technology
Atlanta, GA 30332-0245, USA

 The ORCID identification number(s) for the author(s) of this article can be found under <https://doi.org/10.1002/adma.202001466>.

DOI: 10.1002/adma.202001466

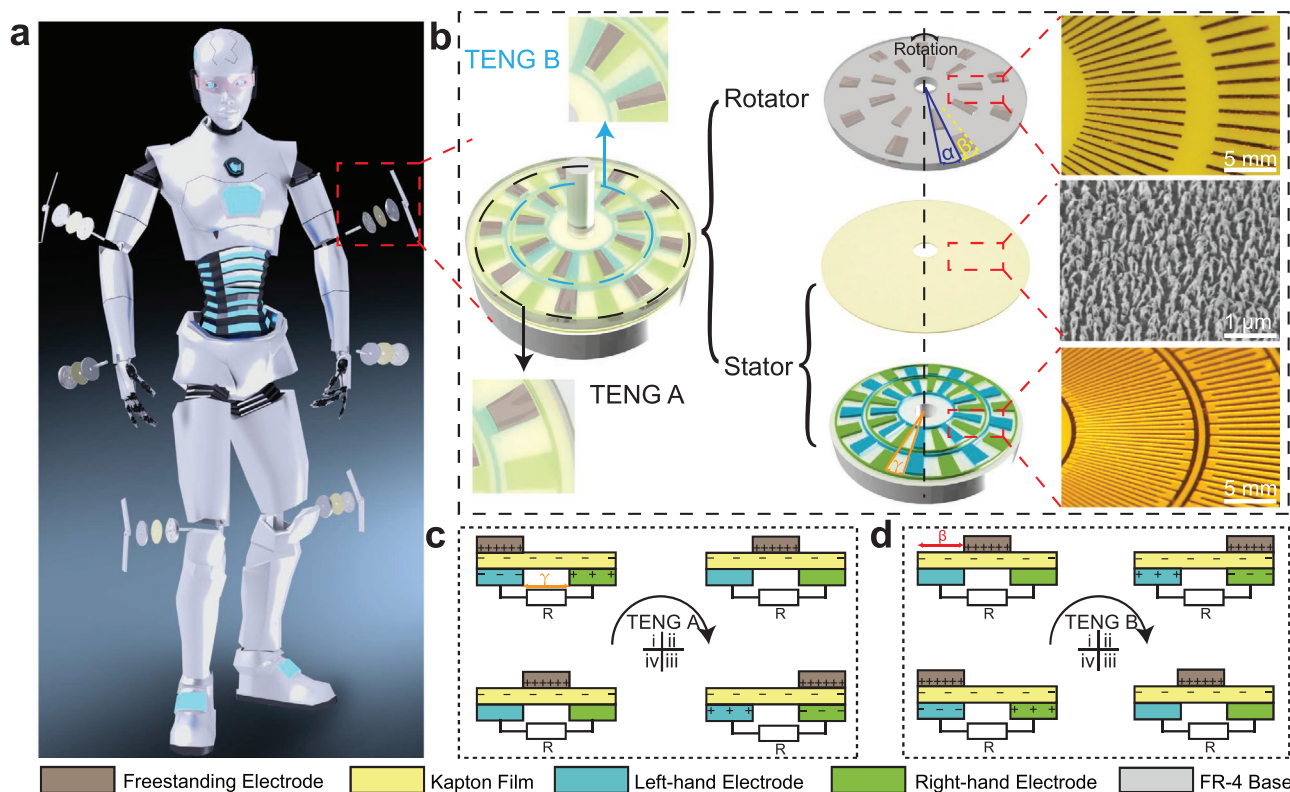


Figure 1. Application, architecture and mechanism of the SPAS. a) The concept of applying SPAS in robotics. b) Detailed structural information of SPAS, which consists of two TENGs: the outer part is named as TENG A (indicated in black) while the inner part is TENG B (indicated in blue). The SPAS can also be regarded as a combination of a rotator and a stator, listed from top to down. The rotator includes an FR-4 base and two groups of radial freestanding electrodes. The central angle of both groups of electrodes is α , and there is a central angle difference of β between them. The stator is composed of a 35 μm thick Kapton film and two groups of radial interdigital electrodes on the top surface of an FR-4 base. There is no central angle difference between two groups of electrodes in the stator. Besides, the central angle of trenches between every two adjacent interdigital electrodes is defined as γ . Images highlighted by red dashed lines are digital photos of the rotator, a scanning electron microscopy (SEM) image of etched nanorods on the Kapton film, and an optical picture of the stator, respectively, from top to down. c) Illustrations of the working principle of TENG A under short-circuit condition when rotating clockwise. d) Schematics of the operating principle of TENG B under the same condition as in (c).

elaborately designed.^[15] Consequently, there still lacks of a self-powered angle sensor with a reliable angle sensing mechanism and improved angular resolution.

Here, we report a self-powered angle sensor (SPAS) with merits of light weight, thin thickness and low cost. The highest resolution (2.03 nano-radian) and sensitivity (5.16 V/0.01°) as well as an unprecedented signal-to-noise (SNR) ratio (98.68 dB) were achieved after a comprehensive optimization. Constructing angle sensing systems based on the SPAS could minimize energy consumption since the generation of sensing signal requires no power supply and the magnitude is high enough that needs no additional amplification. In addition to systematic investigations combining with theoretical analysis were conducted to reveal the sensing mechanism, we had also demonstrated that, equipped with the SPAS, a palletizing robotic arm could precisely reproduce traditional Chinese calligraphy via angular data collected by the SPAS. And the SPAS could also record the flexion/extension of joints after assembled in a medicare brace, which might benefit personalized orthopedic recuperation. Our study establishes a new generation of angle sensors that has broad applications in robotics, medicare, IoT, and artificial intelligence.

The construction of the self-powered angle sensor (SPAS) is based on the newly developed triboelectric nanogenerator (TENG) technology. Benefited from its salient features of light weight and thin thickness, the SPAS is capable of being incorporated with joints in robots without interferences from their rotation/movement.^[16] Figure 1a depicts its expected extensive applications in robotics for high-resolution angular monitoring. Detailed structural information of the SPAS is visualized by Figure 1b. Two rotary contact-sliding mode TENG devices are integrated together, and a difference in the overlaps of electrodes between TENG A and B is designed to generate a set of quadrature signals for sensing. To be specific, from top to bottom, the SPAS consists of a rotator part and a stator part, coaxially assembled. The rotator mainly includes two groups of freestanding electrodes (made up of copper with a thickness of 50 μm). Each group is composed of radially-arrayed electrodes with a central angle of α . Additionally, a central angle difference of β exists between these two groups of electrodes. The stator part consists of a Kapton film (DuPont, thickness of $\approx 35 \mu\text{m}$) which works as the electrification layer and two groups of interdigital electrodes (made up of copper with a thickness of 50 μm). The central angle of each electrode is the

same as that of electrodes in the rotator part. It is noteworthy that no central angle difference between the two groups of electrodes exists, which gives rise to the aforementioned dissimilar overlaps between two TENGs. Another structural parameter γ is defined as the central angle of trenches between every two adjacent interdigital electrodes. Enlarged views of each part are highlighted by red lines. A detailed description of the fabrication procedure is available in the Experimental Section.

Basic units in TENG A and B are selected to elucidate the working principle of the clockwise-rotated SPAS under short-circuit conditions, as shown in Figure 1c,d. Schematics of the contrary direction is depicted in Figure S1a,b (Supporting Information). Freestanding electrodes are positively charged by triboelectrification, with an equal amount of negative charges generated on the Kapton film.^[17] Exemplified by TENG A (Figure 1c), electrostatic induced negative charges are accumulated on the left-hand electrode, while the right-hand electrode is positively charged with an equal amount at the initial state. Movements of joints bring about relative rotation between the rotator and stator, and free electrons will keep flowing from the left-hand electrode to the right-hand one before the freestanding electrode is precisely above the right-hand electrode.^[18] Owing to the difference in overlap, the freestanding electrode in TENG B is ahead of that in TENG A, forming a detectable phase difference between two signals.

To quantitatively deduce the charge distribution on each electrode, a simplified parallel-plate capacitor model can be reasonably introduced in this analysis since the thickness of Kapton film is much smaller than its width and length scale.^[19] According to the triboelectric series, the triboelectric charge densities on the Kapton film is supposed to be $-\sigma$. Combining with the law of charge conservation and basic electrical principles in short-circuit situation, the quantities of charges induced on the left-hand (Q_L) and right-hand (Q_R) electrodes can be calculated by the following equations^[20]

$$Q_L = -Q_R = -Q(\theta) = -\frac{\sigma_o(\theta) \cdot S}{1 + \frac{\alpha}{\alpha - \theta}} \quad (0 \leq \theta \leq \alpha) \quad (1)$$

$$Q_L = -Q_R = -Q(\theta) = \frac{\sigma_o(\theta) \cdot S}{1 + \frac{\alpha}{\theta - \alpha}} \quad (\alpha < \theta \leq 2\alpha) \quad (2)$$

$$\sigma_o(\theta) \cdot \frac{(\alpha - \theta)}{\alpha} \cdot S + \sigma_{uo}(\theta) \cdot \frac{\theta}{\alpha} \cdot S = 3\sigma S \quad (3)$$

where S represents the tribo-surface area of a freestanding electrode, and θ is the angle that the freestanding electrode has rotated by. The charge density of the overlapped area on the bottom surface of the freestanding electrode is defined as $\sigma_o(\theta)$, and the unoverlapped area as $\sigma_{uo}(\theta)$. The whole derivation process and verification of equations listed above are explicated in Note S1 (Supporting Information). Qualitative deduction of open-circuit performance is based on the model of volume-changing capacitors and available in Note S2 (Supporting Information).

Owing to the drift in induced charges between the left-hand and right-hand electrodes is forbidden in an open-circuit condition, the open-circuit voltage (V_{oc}) is thus defined

as the potential difference between these two electrodes, that is, $V_{oc} = V_R - V_L$. Figure 2a depicts the finite element method simulated (COMSOL Multiphysics) open-circuit potential distribution on electrodes under a clockwise situation. In this illustration, to concisely manifest the variation tendency of electric potential, dimensional parameters of the SPAS are selected as $\alpha = \beta = \gamma = 45^\circ$, and corresponding 3D structural schematics are exhibited below. The whole process and that of the reversed direction are also animated in Movies S1 and S2 (Supporting Information), respectively. Clearly can we discover that the potential of one electrode will reach its maximum when the freestanding electrode is precisely above it. Therefore, according to the definition of V_{oc} , the voltage variation trend of TENG B is ahead of TENG A by an angle of 45° (i.e., α), and the period of potential variation for both TENGs is 180° (i.e., 4α). Schematics of the opposite rotary direction are described in Figure S1c (Supporting Information). Numerically calculated open-circuit voltages of two TENGs versus rotational angles under clockwise rotation are plotted in Figure 2b. The voltage of TENG A is indicated by the solid line while that of TENG B by the dashed one. Parameters employed to proceed simulations are listed in Table S1 (Supporting Information), and the calculated profile for the anticlockwise situation is depicted in Figure S1d (Supporting Information). Apart from waveforms under the condition of $\alpha = \beta = \gamma = 45^\circ$, other situations as $\alpha = \beta = \gamma = 10^\circ$ and 1° are investigated and shown together. In these situations, no matter the value varies, the voltage periods of two TENGs are the same (i.e., 4α), and the signal of TENG B is indeed lead by an angle of α in phase, which is consistent with our observation in Figure 2a. Another essential propensity we shall notice in Figure 2b is that a decline of the peak-to-peak value of the simulated voltage is accompanied by an increase in counts per rotate (CPR) when values of α decrease from 45° to 1° . To achieve the best device performance, relationships between central angles and magnitudes of voltages as well as the CPR are revealed by Figure 2c. A dramatic drop of CPR appears with a rise in the open-circuit voltage simultaneously when α merely increases from 1° to 5° . Considering a more reliable approach for angle sensing is via counting numbers of pulses, as a consequence, $\alpha = 1^\circ$ is selected to realize the enhancement in CPR, yet with an inevitable decrease in the magnitude of signals. Fortunately, however, optimization of intervals separating interdigital electrodes which we defined as γ is an effective method to improve open-circuit voltages without a significant sacrifice of CPR.^[21] Here, to intuitively reveal the influence on the peak-to-peak values of voltage caused by the width of intervals, we define the approach to normalize voltage signals as follows

$$V_{\text{Normalized}} = \frac{V}{V_{\gamma}|_{\alpha=0.2}} \quad (4)$$

Simulated relationships between various ratios of γ/α with different values of α and the normalized open-circuit voltage are presented in Figure 2d. Although a monotonical increase of V_{oc} is observed while the ratio of γ over α ascends from 0.2 to 1 for all listed values of α , the increment of normalized voltages when $\alpha = 1^\circ$ is much more dramatic than other conditions: The normalized voltages soared dramatically by 8.17-fold,

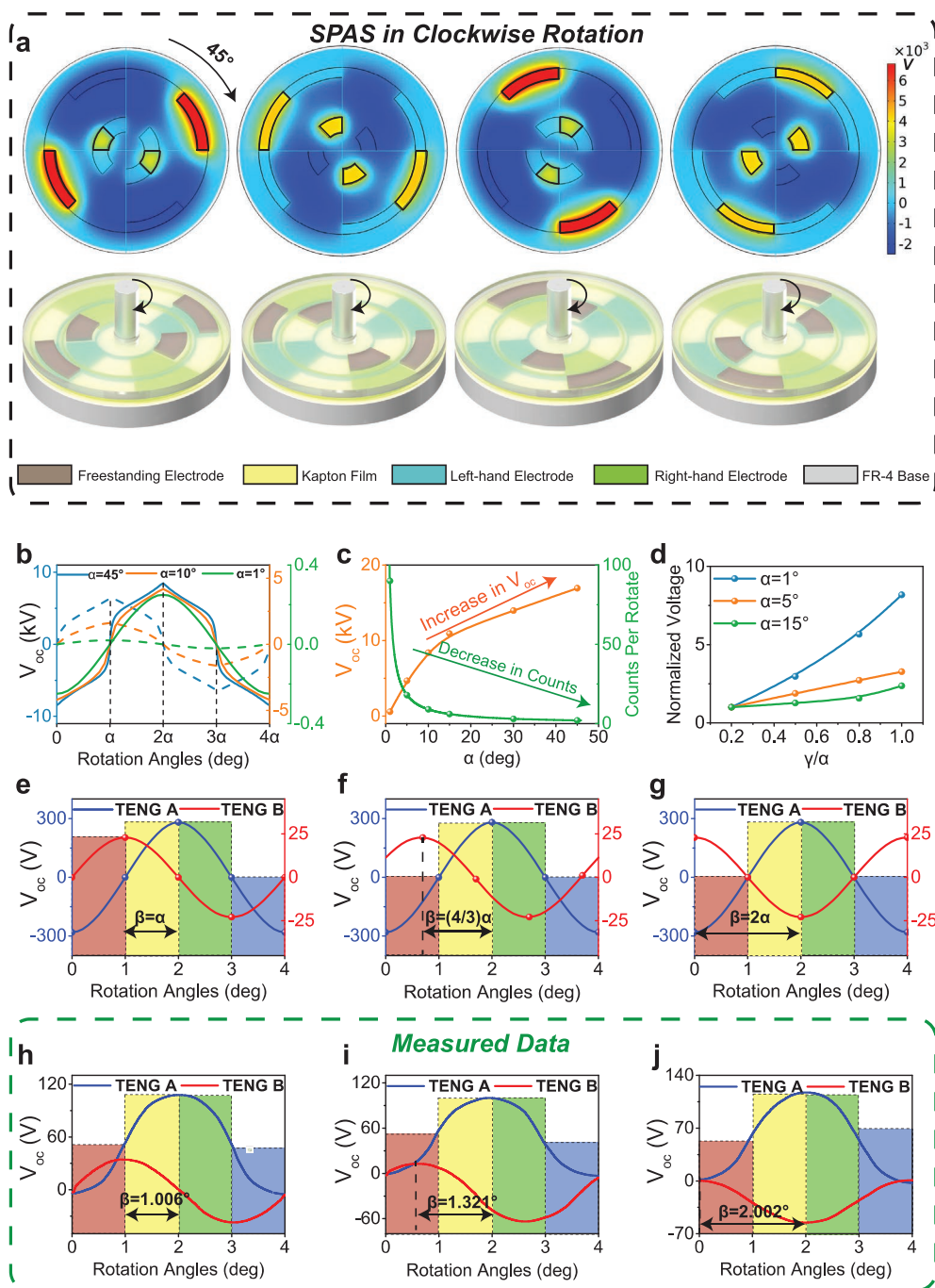


Figure 2. Structural optimization via finite element analysis and experimental verification. a) A top view of the simulated potential distribution profiles of the SPAS in clockwise rotation under the condition of $\alpha = \beta = \gamma = 45^\circ$. Exhibited below are corresponding 3D structural schematics. b) Simulated variations of potential differences of the clockwise rotated SPAS. Variations of TENG A is indicated by the solid line, while that of TENG B by the dashed line. c) Numerical simulation results of variances on the magnitude of open circuit voltage and counts per rotate when α increases from 1° to 45° . d) The simulated relationship between normalized voltages and the ratios of γ over α for several values of α . e–g) Simulated variances of open circuit voltages of clockwise-rotated SPAS in a period with the ratios of β over α equal to 1, 4/3, and 2 respectively. The values of α and γ are both restricted to 1° , the optimum value. h–j) Corresponding experimental verification of simulated results in (e–g).

while the CPR merely decreased by 1.67-fold (Table S2, Supporting Information). The signal-to-noise ratio (SNR), defined by the strength of desired signal compared to the undesired background noise, is also a significant character for sensors. Therefore, an optimal option of structural parameters of SPAS

is selected as $\alpha = \gamma = 1^\circ$ to achieve a balance between the magnitude of sensing signals and the CPR.

Another geometric parameter to be optimized is the central angle difference (β) existing between two groups of free-standing electrodes on the rotator part. Since the variation

of β will not interfere with previous conclusions, we proceed simulations with a combination of several values of β under the restriction of $\alpha = \gamma = 1^\circ$ (Figure S1e,f, Supporting Information). As depicted from Figure 2e–g, TENG B advances more in phase comparison as the ratio of β over α arises from 1 to 2 when in clockwise rotation. To quantify the extent of phase lead, the connection between β and phase difference is investigated. Theoretically, the period of voltage signal spans 4α degrees which are equivalent to 360° in phase, so that a value of β equal to $n \cdot \alpha$ is inferred to a $90 \cdot n$ -degree lead in phase comparison. A set of quadrature signals is favorable in the sensor field in that it is capable of achieving a more precise angular resolution merely by signal processing methods. Hence, the overall optimization conclusion of dimensional parameters is $\alpha = \beta = \gamma = 1^\circ$.

In addition to finite element analysis, experiments of the same device size and rotation condition were also carried out. Measured data are plotted from Figure 2h–j, which exhibits almost the same profiles and phase difference compared to the simulated results (Figure 2e–g), validating our theoretical premises mentioned above. The phase differences in Figure 2h–j only deviate from predicted results with a relative error of

0.58%, -0.68% , and -0.35% respectively. Specific information is available in Table S3 (Supporting Information). The higher voltage magnitude of TENG A is mainly ascribed to the tribo-surface of TENG A is larger than that of TENG B. Theoretical and experimental results of the reversed direction are depicted in Figure S1g–l (Supporting Information).

A closed-loop rotary platform was established to systematically characterize the SPAS under various rotation conditions (Figure S2a and Movie S3, Supporting Information). Since angular information including rotation angles and angular velocities can be obtained by a single TENG in the SPAS, we first focus on the open-circuit voltage signal of the TENG A (Note S3, Supporting Information). Figure 3a,b are two preliminary experiments for validating the mechanism of the SPAS. In Figure 3a, the SPAS was rotated by various overall rotation angles at a certain angular velocity of 1° s^{-1} . Although the initial state was randomly chosen, profiles of measured voltage data will span a complete period as long as the overall rotation angle increases by 4° . Therefore, by counting the number of pulses, we can obtain the overall rotation angles. Moreover, the angular velocity can be derived from dividing the rotation angle with the spent time. Since the device structure is entirely symmetrical, the

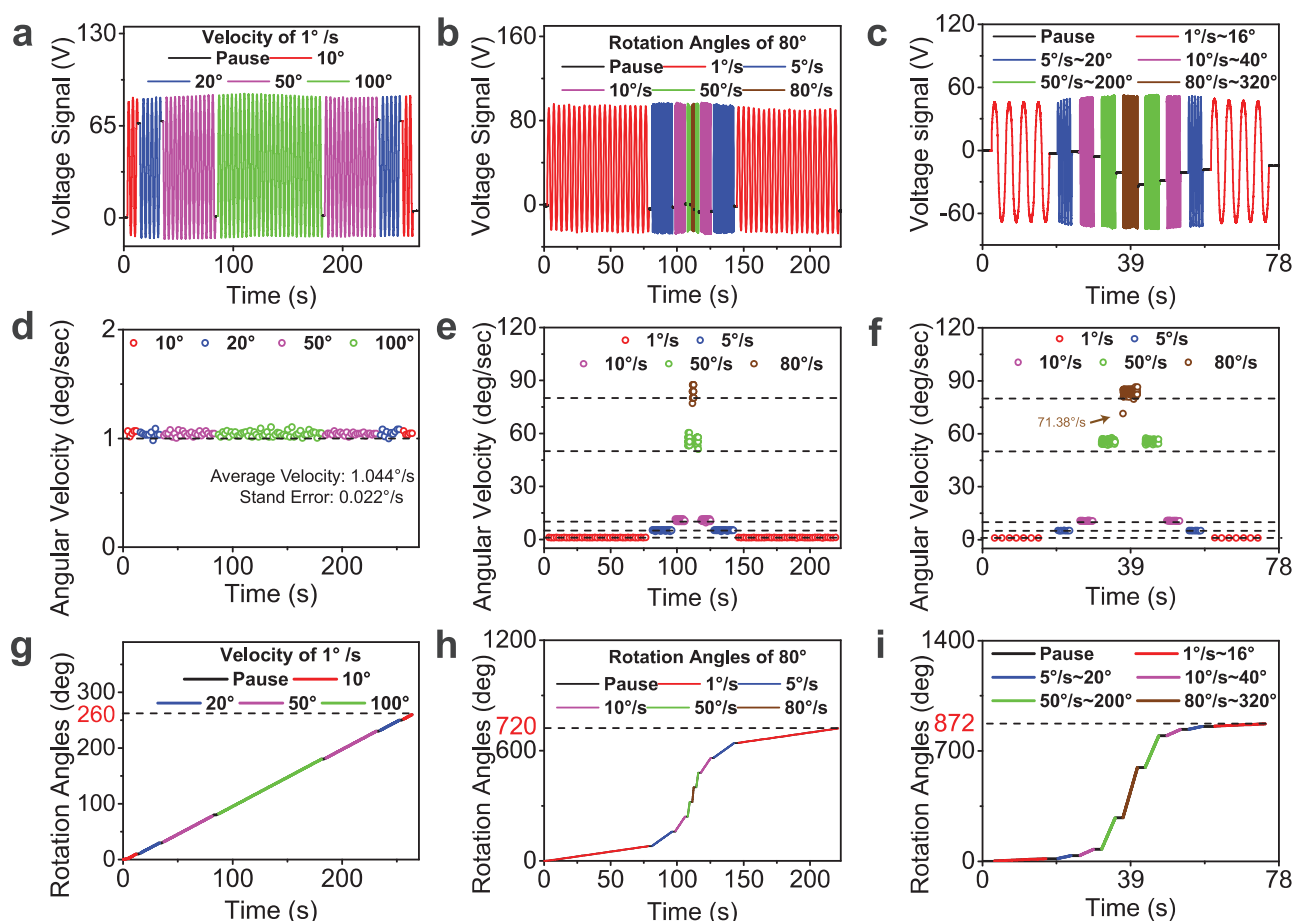


Figure 3. Characterization of SPAS. a) Voltage signals generated at the angular velocity of 1° s^{-1} with various overall rotation angles. b) Voltage signals under different angular velocities with a given overall rotation angle of 80° . c) Voltage profiles under different combinations of overall rotation angles and angular velocities. d–f) Calculated angular velocities from the experiment data in the diagram (a–c), and their comparisons with the pre-set one. g–i) plot the overall rotation angles over time under the same operations in (a–c), respectively.

angular resolution can be improved to 2° via the introduction of the crest point (Figure S2b, Supporting Information). Magnified illustrations of this process are available in Figure S2c–e (Supporting Information). The subsequent investigation focuses on the waveform under various angular velocities ranging from 1 to 80° s⁻¹, with a fixed overall rotation angle of 80°. As demonstrated by Figure 3b, an identical number of voltage pulses of 20 was obtained under all velocities (Figure S2f–h, Supporting Information), which suggests an irrelevance between the number of signal pulses and the angular velocity. Afterward, a comprehensive experiment composed of various overall rotation angles with different angular velocities was conducted. The legends in Figure 3c describe the detailed scenarios in this experiment. Profiles of each stage are in entire accordance with previous conclusions (Figure S2i–k, Supporting Information). Note: the output voltage is so high that no amplification is needed, and it is independent of rotation frequency, which is validated by Figure S2l (Supporting Information).

Figure 3d–f exhibits angular velocities calculated with data plotted in Figure 3a–c via strategies stated above, inserted dashed lines denote pre-set angular velocities. Calculated angular velocities fluctuate around the pre-set one with an averaged velocity of 1.044° s⁻¹ and a standard error of 0.022° s⁻¹ in the case of Figure 3d. Calculated velocities in Figure 3e,f are also accord with pre-set values. The deviation of calculated results when angular velocities beyond 50° s⁻¹ is mainly attributed to the roughness of tribo-layer and a lack of the velocity feedback control circuit in this platform. The existence of an apparent low value pointed by an arrow in Figure 3f is ascribed to that the motor reaches its maximum acceleration. Illustrations presented from Figure 3g–i demonstrate calculated rotation angles changing with time under identical conditions in Figure 3a–c, separately. The highest value represents the pre-set overall rotation angle, and the angular velocity determines the type of the curve. Providing that the influence on line types caused by the pause time is negligible, the waveform of the curve plotted in Figure 3g resembles a straight line and waveforms of Figure 3h,i are similar to a typical “S-curve,” which is also consistent with our preset velocity. The accordance both in angular velocity and overall angles proves the feasibility and accuracy of the SPAS.

In spite of rotation angles and angular velocities have been attained by a single TENG, unfortunately, however, the direction of rotation, another vital parameter in practical applications, cannot be obtained yet (Figure S2m,n, Supporting Information). Hence, TENG B is introduced to produce a reference signal. A multichannel synchronous data acquisition system is employed to record signals produced by two or more TENGs simultaneously (Figure S3a, Supporting Information). Figure 4a explicates waveforms of two TENGs measured simultaneously on condition that an anticlockwise rotation is followed by a clockwise one. Signals belonging to TENG A and B are regarded as sensing and reference signals, and plotted in blue and red, respectively. Moreover, the generated quadrature signals under anticlockwise rotation are highlighted by yellow while clockwise rotation by green. An apparent and consistent discrepancy in phase is clearly revealed by the enlarged views of voltage signals under both rotary conditions. Besides, since positions of crests or troughs

of the reference signal are intermediate points between that of the sensing signal (Table S4, Supporting Information), angular resolution can be further enhanced to 1°, i.e., the central angle of electrodes (Figure S3b, Supporting Information). It is inferable that developing new fabrication methods with a reduced central angle of electrodes will lead to a higher angular resolution of SPAS.

The robustness of SPAS was investigated and exhibited in Figure 4b,c. The width of peaks fluctuates around 4° with a maximum standard error of 0.0508° and the counts per rotate is stabilized at the number of 90 as angular velocities varying from 1 to 80° s⁻¹, which indicates the stability of signals in a large angular velocity range. This is mainly attributed to the noticeable merit of grating structure TENGs that local surface defections will not affect a single voltage pulse. Besides, highlighted by orange in Figure 4c is a cyclic test of 100 000 cycles to confirm the reliability of sensing signals during long-lasting operation. An average open-circuit voltage of 123.09 V along with a standard error of 0.48 V was obtained during this test, and no obvious decrease in the magnitude of signal was found. Slight undulations of the open-circuit voltage can be mainly ascribed to the trivial unevenness of the contact surface.

Other than the scheme we discussed above to obtain rotation angles, a substantial enhancement of the angular resolution is realized by a detailed analysis of signals within a single period. As shown in Figure 4d, voltages within the range from 2.70° to 3.25° can be mathematically linearized with the adjusted *R*-square of 0.99808, which represents a linear error less than 0.2% is achieved. A step rotation experiment with every step of 0.05° was employed to discover the highly-sensitive area within a voltage period. Inside the linear area, a highly-sensitive region is explored to be in the range from 2.95° to 3.10° as exhibited by the red dashed rectangle in Figure 4e. Within this linear and highly sensitive region, every step rotation of 0.01° could be evidently distinguished with an average voltage variance of 5.16 V as presented in Figure 4f, and a response time of 57 ms (Figure S3d, Supporting Information). Since the Root Mean Square (RMS) of the noise signal is 0.06 mV as shown in the inset of Figure 4f, a minimum resolvable angle of 2.03 nano-radian is achieved within this range via the following expression^[22]

$$A = \frac{\Delta A}{\Delta V / V_{\text{Noise}}^{\text{RMS}}} \quad (5)$$

where *A* is the minimum resolvable angle, ΔA is the rotation step, ΔV is the voltage variance corresponding to ΔA . In addition, the signal-to-noise (SNR) ratio related to this region is calculated to 98.69 dB through the subsequent formula^[23]

$$\text{SNR} = 20 \cdot \lg \frac{V_{\text{Signal}}^{\text{RMS}}}{V_{\text{Noise}}^{\text{RMS}}} \quad (6)$$

It is noteworthy that the angular resolution and SNR ratio can be further enhanced by the improvement of the magnitude of the voltage signal. In all, above-mentioned sensing characteristics demonstrate the advantage and feasibility of constructing a self-powered angle sensor based on the TENG technology.

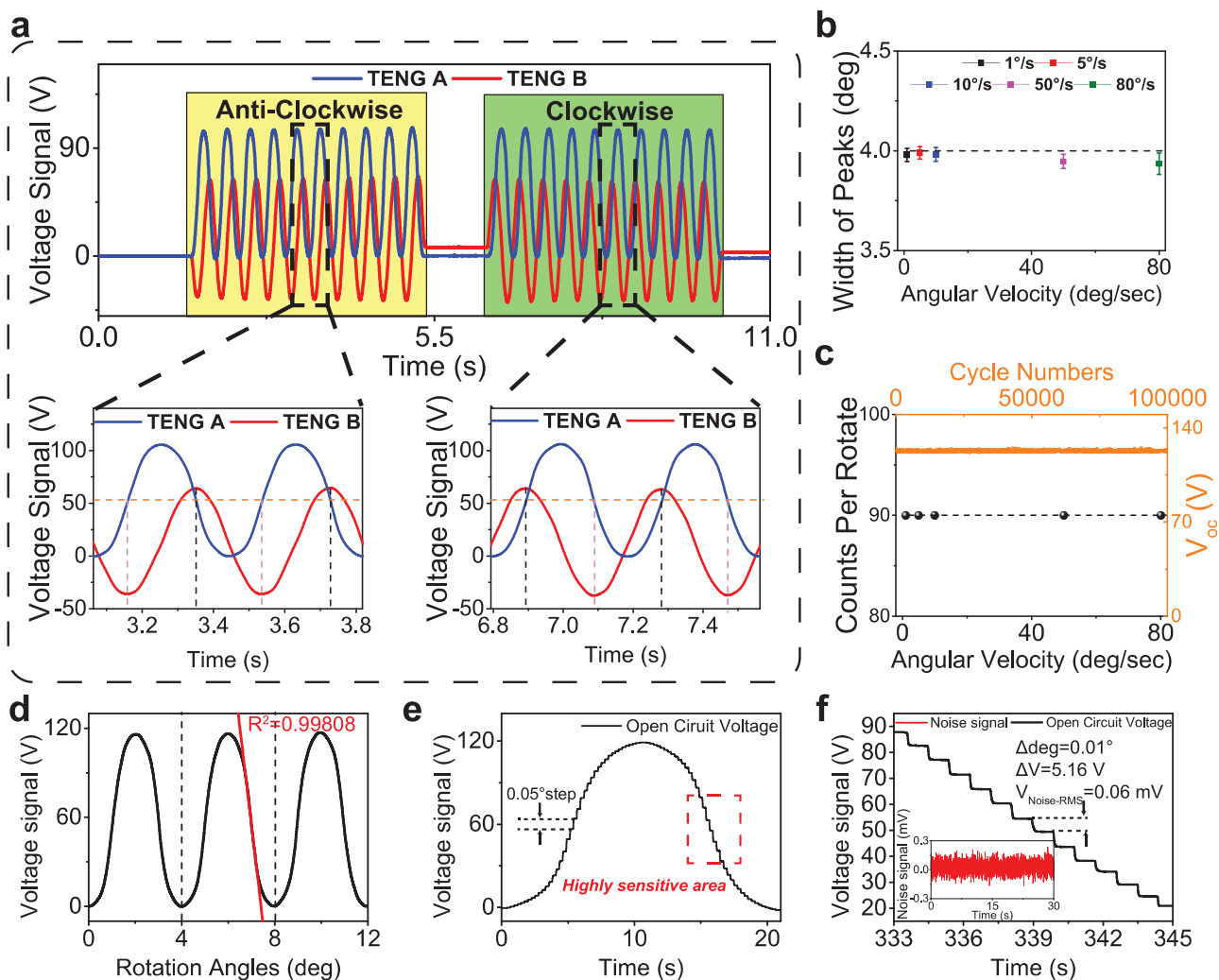


Figure 4. Detailed analysis of sensing signals. a) Voltage signals generated when the device proceeds anticlockwise rotation followed by a clockwise one, the inserted images are enlarged views of distinct phase differences between TENG A and B. b) Statistic results of the width of peaks under various angular velocities, the inserted dotted line lies on the position of 4° . c) Measured counts per peaks at different angular velocities and the stability of open-circuit voltage during 100 000 cycles. d) The shape of the voltage signal within a period is highly repeatable, and an excellent linear area is shown inside each period with a value of adjusted R^2 of 0.99808. e) A profile of the measured open circuit voltage with a step rotation of 0.05° per step within a period. The highly sensitive region is highlighted by the red dashed rectangle. f) Voltage signals with a rate of 0.01° per step inside the linear and highly sensitive area. The inset is the waveform of the noise signal. Considering the RMS value of the noise signal is 0.06 mV, and the voltage variation corresponding to 0.01° is 5.16 V, the minimum resolution can be calculated to 2.03 nano-radian.

It is of vital importance for robots to accurately acquire joints' real-time positions via the most energy-efficient method in practical applications where the power supply is usually limited. Our SPAS could realize it by directly assembling in, since its structure is simple and neither external power nor amplification module is required for the generation of sensing signal. A palletizing robotic arm equipped with SPASs on each of its three joints is constructed to demonstrate the practicability, as presented in Figure 5a and Figure S4a (Supporting Information). Owing to the merits of lightweight (11.1 g) and thin thickness (1.87 mm) (Figure S4b, Supporting Information), the integrated SPASs would not affect the joints' rotation/movement. Geometric parameters of the three SPASs are listed in Figure S4c (Supporting Information). Vividly depicted in Figure 5b are two processes utilized for this verification: After we input a

trajectory of a calligraphic script, the robotic arm will follow it to move. Meanwhile, motion-induced voltage signals will be generated and collected. In the subsequent process, the robotic arm will duplicate the calligraphy based on the recorded data (Movie S4, Supporting Information). At last, a contrast between these two calligraphic results is given.

Figure 5c is a screenshot of the multichannel data acquisition program developed on the LabVIEW platform with six channels working during process 1. Denotations represented by each channel are available in Figure 5d which also serves as a magnified picture of the selected area in the previous image. Basically, the magnitude and peak number of voltage signals represent a certain angular variation, whereas the rotational direction can be obtained by the phase difference. The principle concerning translates voltage signals into angular data

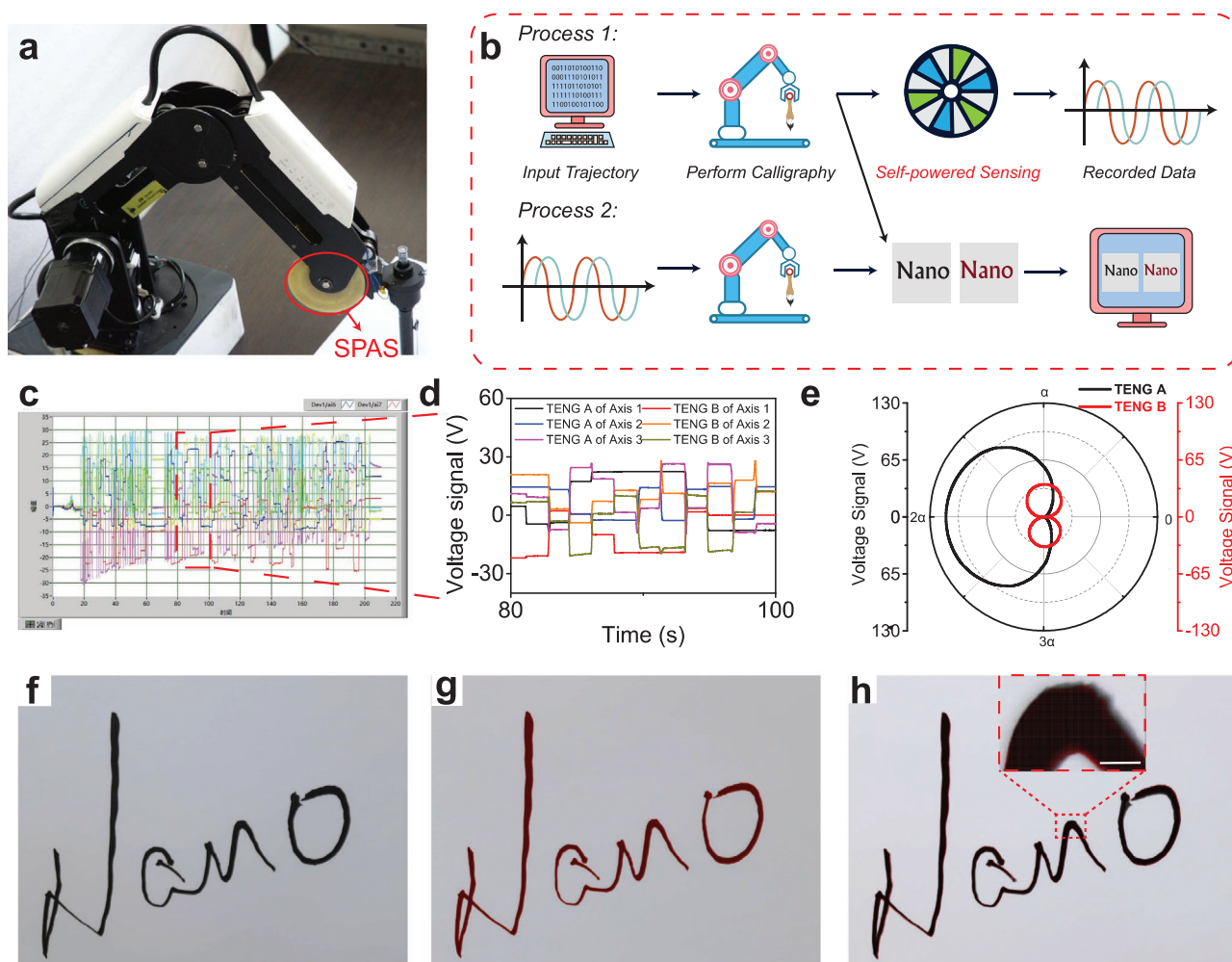


Figure 5. Demonstration of applications of SPAS in real-time high-resolution angular monitoring in robotics. a) The digital photo of a three-axis robotic arm equipped with SPAS around its joints. b) Schematic illustration of recording real-time high-resolution data by SPAS during a robotic arm performs traditional Chinese calligraphy through tracking inputted trajectory (Process 1) followed by repeating the whole action with the collected data, and then comparing these two calligraphy results using digital methods (Process 2). c) A screenshot of the collected voltage data during Process 1. d) A magnified image of the selected area in diagram (c) to exhibit the recorded six-channel voltage data in real-time. e) A polar plotted graph of voltage signals generated by SPAS in a period to illustrate the correspondence between angular data and voltage signals. f) The original calligraphy completed by the robotic arm. g) The duplicated calligraphy performed from the recorded data. h) A comparison between these two results of calligraphy through overlapping, the inset demonstrates the tiny difference of two results. Scale bar, 200 μm .

is exhibited by Figure 5e. In this depiction, a polar coordinate representation of the voltage signals is utilized to intuitively reveal the correspondence between angular positions and generated signals, which is specified in the Experimental Section.

Presented in Figure 5f is the original calligraphy of the word “Nano” through the trajectory, while Figure 5g depicts the duplicated calligraphy based on measured data. A close comparison between these two calligraphic scripts is given by overlap as depicted by Figure 5h (the original in black, and the duplicated in red). An almost entire superposition of two calligraphic tracks is observed while a minute difference of stroke width exists, which is mainly ascribed to that the tip of the ink brush might vary slightly during the writing process. Figure S4d (Supporting Information) provides further verification of identicalness of scripts through comparison between pixels. Inserted in Figure 5h is an enlarged view of the comparison

result around the corner of letter “n,” proving that scripts overlap well with each other in a majority of the area: Only a 20 μm difference in the width scale exists. This demonstration vividly exhibits the remarkable practicability of applying the SPAS to robotic arms for precisely monitoring angular positions of each joint.

Apart from serving as a high-resolution angular monitoring system for robotic arms, the SPAS can also be utilized on actively recording daily flexion/extension angles of joints. Approximate 22.7% of adults in the U.S. suffer from arthritis or arthritis-attributed activity limitation (AAAL), and this ratio soars to 49.7% as the age beyond 65.^[24] Fortunately, however, doctors could personalize recuperation schedules with the assistance of daily extensions/flexions data of joints, and the associated limitation can be alleviated via the aid of emerging rehabilitation robots.^[25] Considering the SPAS is an active

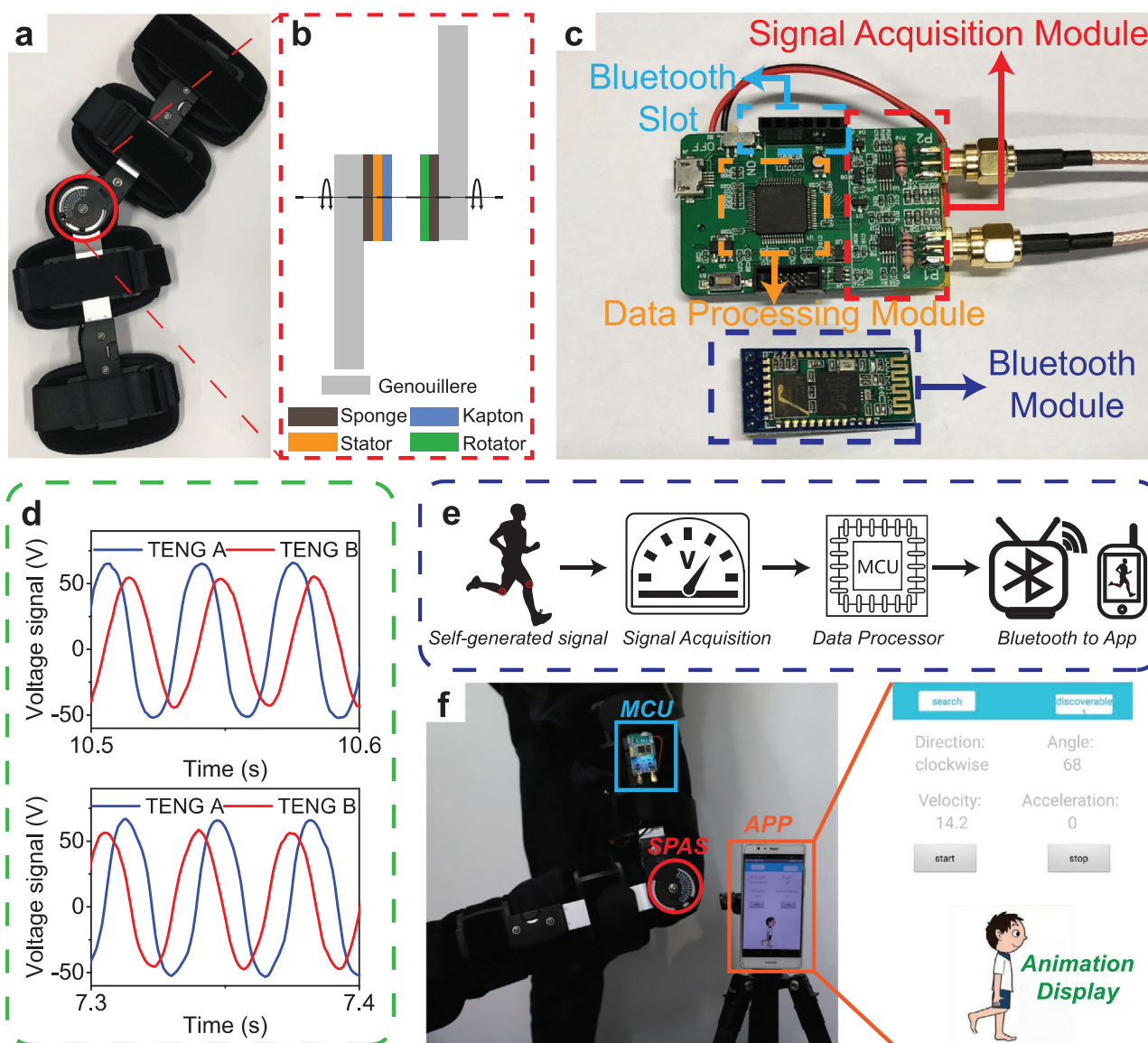


Figure 6. Medical application of the SPAS for personalized orthopedic medicare. a) A digital photo of a personal brace incorporated with the SPAS. b) A lateral illustration of the integrated device. c) An optical image of the MCU we devised for portable purpose. d) Waveforms of the signals measured by the devised MCU when the SPAS rotate clockwise and anticlockwise, as listed from top to down. e) Schematics of the operating mechanism of the “active bending measurement” system. f) Demonstration of applying the SPAS for recoding joints’ flexion/extension angles, the inserted picture is a screenshot from the App we developed for the mobile phone to visualize the status of joints.

sensor and its sensing signal is high enough that needs no additional amplification, developing a high-resolution angle sensing system based on SPAS could realize minimized energy consumption during operation, which is of crucial significance for the long-lasting practical application.

The integration of SPAS with a traditional personal brace is shown by **Figure 6a**. A schematic depiction from the lateral view is available in **Figure 6b** to illustrate its structural information. In order to satisfy the requirement of mobility, we developed a microcontroller unit (MCU) with a size of 3×5 cm to complete the signal acquisition, data processing and results transmitting via Bluetooth, as depicted by the optical photo in **Figure 6c**. The detailed circuit diagram is available in **Figure S5a** (Supporting Information). The incorporation of above-mentioned

devices constitutes an active bending measurement system (ABM system) which could actively sense and record extension/flexion states of joints. To verify the feasibility of this circuit, we measured the analog signal output and plotted it in **Figure 6d**, indicating that the relationship between phase difference and rotary direction is entirely consistent with previous conclusions, and the shape is still highly repeatable over periods too. A large dynamic measurement range from 20 to 150° s^{-1} is achieved after an overall optimization of the MCU (Movie S5, Supporting Information), which contains the angular velocities of joints required to accomplish a majority of actions,^[26] implying possible applications of the ABM system not only in the rehabilitation field but also for the emerging exoskeletons.^[27] **Figure 6e** intuitively shows the operating procedures of the “ABM brace.”

As vividly depicted in Figure 6f, while an experimenter bending his/her knee with the brace on, the flexion/extension status of the joint is simultaneously recorded by the SPAS, transmitted by the MCU, and visualized by the APP. The inserted image is an enlarged view of the APP, in which the top part lists four vital motion parameters in real-time, and an instantaneous animation display of the status of joints is available at the bottom. Moreover, a series of experiments with various flexion/extension angles and velocities were performed and available in Movie S6 (Supporting Information). Comparisons of signal magnitude and electricity rely between the SPAS and a traditional angle sensor (GTS06, GTEACH Inc.) is exhibited in Movie S7 (Supporting Information). Detailed information of the traditional sensor can be found at Table S5 (Supporting Information). This attempt of integration the SPAS with medicare brace not only indicates the viability of constructing an active sensor system for personalized recuperation in the era of IoT, but also implies the potential of applying the SPAS to the next generation of rehabilitation robots.

In summary, we have constructed a SPAS based on the newly developed TENG technology, which exhibits merits of both light weight and low cost, as well as unprecedented sensitivity and SNR ratio. Neither additional electric power supply nor signal amplification module is required for SPAS, which largely facilitates its extensive integrated applications, such as robotics and rehabilitation medicare in this work. Besides, via micro/nano fabrication methods and the enhancement of sensing signal, the device can be further improved, including the device volume, weight, as well as the resolution. The merits mentioned above and the feature of no extra energy consumption may indicate a novel approach for constructing active angle measurement systems with minimized energy consumption to meet challenges arose from robotics, personalized medicare, artificial intelligence and the era of IoT.

Experimental Section

Fabrication of the SPAS: The fabrication of the SPAS is mainly based on the mature printed circuit board (PCB) technology. Thus, schematic illustrations of SPAS's multilayer structures are necessary previous to the automatic production. An electronic structural design software named of Altium Designer 16 was used to depict the structural sketches which are available in Figure S5b (Supporting Information). Detailed fabrication procedures are revealed as follows: The substrate chosen for both the rotator and stator is FR-4 epoxy glass with a thickness of 1 mm. To transfer patterns of copper to this substrate, first it was covered with a complete copper sheet with a thickness of 50 μm on FR-4 base through cold rolling craft followed by laminate a sensitive dry layer on the top of the copper sheet. After that, the sensitive layer is exposed to patterned UV light via photo tools, and the unexposed part of this layer is removed by the developing solution. Previous to the strip of the dry film layer, redundant copper is etched by ferric chloride solution and removed from the patterned copper. Finally, a Kapton film with thickness around 50 μm is attached to the stator part to function as a triboelectric layer while a layer of gold is deposited to the surface of patterned copper of the rotator part to prevent copper from oxidation.

Experimental Setup for Rotational Parameters Control: A closed-loop servo motor was required to drive a rotating platform (NDG85, USC corporation) which was installed on an optical table (OTSB345-1, Zolix corporation). To precisely control rotational parameters, a reduction ratio of 18 was devised, and all combinations of parameters were input

to a programmable controller which was directly linked to the motor. Three circular acrylic sheets with a sandwiched-structure were applied as the junction part between the SPAS and the rotation system by using a laser cutter. The rotator and stator sections of the SPAS were attached to the interface between two acrylic sheets where relative rotation exists.

Multichannel Synchronous Electric Signal Measurement and Materials Characterization: For the section of basic output performance tests of the SPAS, several programmable electrometers (6517 from Keithley Instruments) were directly linked to a synchronous data acquisition card (6356 from National Instruments) to simultaneously measure the multichannel OC voltage, SC current or transferred charge signals. These data were collected and saved by a corresponding multichannel data acquisition program which was developed on the LabVIEW platform. A low pass filter (50 Hz) was used in data post-processing of measured signals. Field-emission scanning electron microscopy (Hitachi SU8020) was applied to investigate the surface morphology of induced nanostructures on the surface of the Kapton film.

Illustration of Translating Voltage Variance into Rotation Angles: There are two strategies to obtain rotation angles provided here. The first method is to count the number of occurrences of featured points (peaks, troughs, and intermediate points) and compare the phase difference between the sensing signal and the reference signal. Besides, the second scheme to detect angular movement is via establishing the correspondence between rotation angles and voltage signals within a single period. Angle sensing based on the first approach is more reliable since it is independent of the magnitude of sensing signals, and the second method could provide a more precise angular information due to high outputs and low noise signal, though this approach relies on the magnitude of signals. Specific rules are as follows: Variation in voltage signals from an intermediate point to a crest or a trough is directly counted as 1° and vice versa, however, angular data corresponding to a variance of voltage less than half maximum has to be derived from the correspondence between angular position and the output performance of the SPAS, as explicated by Figure S6a (Supporting Information). Rotary direction is derived from the phase difference between the sensing signal and the reference signal: anticlockwise rotation is corresponding to a phase-lead of sensing signal, while the clockwise rotation is quite contrary.

Strategies for Recognizing Phase Difference: Phase difference can be obtained via comparing the magnitude of sensing signal to a certain value at several special points. To be specific, at the point that its first order derivative reaches the positive maximum, this point is defined as the zero-crossing point during ascent (ZCPDA) and is labelled by orange as depicted in Figure S6f (Supporting Information). Similarly, the point whose first order derivative reaches the negative maximum is regarded as the zero-crossing point during descent (ZCPDD), and highlighted in magenta. In addition, the "zero point" is defined as its value is the half of the sum of that of crest and trough. In the situation that reference signal is phase-leading, when a ZCPDA appears in the reference signal, the value of sensing signal is less than that of "zero point." However, for the ZCPDD, its occurrence is corresponding to the sensing signal shows a larger magnitude at the condition of clockwise rotation. The abovementioned correspondences are exactly reversed in anti-clockwise rotation situation. Thus, the phase difference between these two sets of signals can be distinguished, and further, the rotational direction.

Supporting Information

Supporting Information is available from the Wiley Online Library or from the author.

Acknowledgements

Z.W. and J.A. contributed equally to this work. The authors thank Junyi Yue for his assistance of Inductively Coupled Plasma etching on the surface of the Kapton film. This work was supported by the

National Key R&D Project from Minister of Science and Technology (Grant No. 2016YFA0202704), National Natural Science Foundation of China (Grant Nos. 51432005 and 5151101243), Beijing Municipal Science and Technology Commission (Grant Nos. Z181100003818016, Z171100000317001, Z171100002017017, and Y3993113DF), China Postdoctoral Science Foundation (2019M660766), and Youth Innovation Promotion Association, CAS. The protocol for the detailed experiments involving human volunteers was reviewed and approved by the Committee on Ethics of Biomedicine Research, Beijing Institute of Nanoenergy and Nanosystems. The human volunteer, one of the authors, took part following informed consent.

Conflict of Interest

The authors declare no conflict of interest.

Keywords

Internet-of-Things, personalized healthcare, robotics, self-powered sensors, triboelectric nanogenerators

Received: March 1, 2020

Revised: April 30, 2020

Published online:

- [1] B. Siciliano, O. Khatib, *Springer Handbook of Robotics*, Springer, New York **2016**.
- [2] G. Z. Yang, J. Bellingham, P. E. Dupont, P. Fischer, L. Floridi, R. Full, N. Jacobstein, V. Kumar, M. McNutt, R. Merrifield, B. J. Nelson, B. Scassellati, M. Taddeo, R. Taylor, M. Veloso, Z. L. Wang, R. Wood, *Sci. Rob.* **2018**, *3*, 14.
- [3] a) P. Cheng, B. Oelmann, *IEEE Trans. Instrum. Meas.* **2010**, *59*, 404; b) S. K. Banala, S. Hun Kim, S. K. Agrawal, J. P. Scholz, in *2nd IEEE RAS and EMBS Int. Conf. on Biomedical Robotics and Biomechatronics*, IEEE, Piscataway, NJ, USA **2008**, pp. 653–658; c) S. J. Russell, P. Norvig, *Artificial Intelligence: A Modern Approach*, Pearson Education Limited, Malaysia **2016**.
- [4] a) T. Kojima, Y. Kikuchi, S. Seki, H. Wakiwaka, in *8th IEEE Int. Workshop on Advanced Motion Control*, IEEE, Piscataway, NJ, USA **2004**, pp. 493–498; b) Y. Kikuchi, F. Nakamura, H. Wakiwaka, H. Yamada, *IEEE Trans. Magn.* **1997**, *33*, 3370; c) T. Seel, J. Raisch, T. Schauer, *Sensors* **2014**, *14*, 6891.
- [5] A. Čolaković, M. Hadžialić, *Comput. Networks* **2018**, *144*, 17.
- [6] E. Hittinger, P. Jaramillo, *Science* **2019**, *364*, 326.
- [7] a) H. I. Krebs, J. J. Palazzolo, L. Dipietro, M. Ferraro, J. Krol, K. Rannekleiv, B. T. Volpe, N. Hogan, *Auton. Rob.* **2003**, *15*, 7; b) C. Wu, A. C. Wang, W. Ding, H. Guo, Z. L. Wang, *Adv. Energy Mater.* **2018**, *9*, 1802906.
- [8] a) Z. L. Wang, *Mater. Today* **2017**, *20*, 74; b) F.-R. Fan, Z.-Q. Tian, Z. L. Wang, *Nano Energy* **2012**, *1*, 328.
- [9] a) Z. L. Wang, *Faraday Discuss.* **2015**, *176*, 447; b) C. Ning, L. Tian, X. Zhao, S. Xiang, Y. Tang, E. Liang, Y. Mao, *J. Mater. Chem. A* **2018**, *6*, 19143; c) M. Wang, N. Zhang, Y. Tang, H. Zhang, C. Ning, L. Tian, W. Li, J. Zhang, Y. Mao, E. Liang, *J. Mater. Chem. A* **2017**, *5*, 12252.
- [10] a) J. Nie, Z. Wang, Z. Ren, S. Li, X. Chen, Z. L. Wang, *Nat. Commun.* **2019**, *10*, 2264; b) J. An, Z. M. Wang, T. Jiang, X. Liang, Z. L. Wang, *Adv. Funct. Mater.* **2019**, *29*, 1904867; c) S. Li, Y. Fan, H. Chen, J. Nie, Y. Liang, X. Tao, J. Zhang, X. Chen, E. Fu, Z. L. Wang, *Energy Environ. Sci.* **2020**, *13*, 896; d) J. Nie, Z. Ren, L. Xu, S. Lin, F. Zhan, X. Chen, Z. L. Wang, *Adv. Mater.* **2020**, *32*, 1905696; e) J. Kim, H. Ryu, J. H. Lee, U. Khan, S. S. Kwak, H.-J. Yoon, S.-W. Kim, *Adv. Energy Mater.* **2020**, *10*, 2070040.
- [11] a) A. Y. Li, Y. L. Zi, H. Y. Guo, Z. L. Wang, F. M. Fernandez, *Nat. Nanotechnol.* **2017**, *12*, 481; b) J. Xiong, P. Cui, X. Chen, J. Wang, K. Parida, M.-F. Lin, P. S. Lee, *Nat. Commun.* **2018**, *9*, 4280; c) R. Hinchet, H.-J. Yoon, H. Ryu, M.-K. Kim, E.-K. Choi, D.-S. Kim, S.-W. Kim, *Science* **2019**, *365*, 491.
- [12] a) Z. L. Wang, *Nature* **2017**, *542*, 159; b) U. Khan, S.-W. Kim, *ACS Nano* **2016**, *10*, 6429; c) S. S. Kwak, S. M. Kim, H. Ryu, J. Kim, U. Khan, H.-J. Yoon, Y. H. Jeong, S.-W. Kim, *Energy Environ. Sci.* **2019**, *12*, 3156.
- [13] a) H. Y. Guo, X. J. Pu, J. Chen, Y. Meng, M. H. Yeh, G. L. Liu, Q. Tang, B. D. Chen, D. Liu, S. Qi, C. S. Wu, C. G. Hu, J. Wang, Z. L. Wang, *Sci. Rob.* **2018**, *3*, 9; b) Q. Hua, J. Sun, H. Liu, R. Bao, R. Yu, J. Zhai, C. Pan, Z. L. Wang, *Nat. Commun.* **2018**, *9*, 244; c) Y. Tang, H. Zhou, X. Sun, N. Diao, J. Wang, B. Zhang, C. Qin, E. Liang, Y. Mao, *Adv. Funct. Mater.* **2020**, *30*, 1907893. d) B. Zhang, Y. Tang, R. Dai, H. Wang, X. Sun, C. Qin, Z. Pan, E. Liang, Y. Mao, *Nano Energy* **2019**, *64*, 103953. e) M. Wang, J. Zhang, Y. Tang, J. Li, B. Zhang, E. Liang, Y. Mao, X. Wang, *ACS Nano* **2018**, *12*, 6156.
- [14] W. Xu, L. B. Huang, M. C. Wong, L. Chen, G. X. Bai, J. H. Hao, *Adv. Energy Mater.* **2017**, *7*, 1601529.
- [15] Y. Wu, Q. Jing, J. Chen, P. Bai, J. Bai, G. Zhu, Y. Su, Z. L. Wang, *Adv. Funct. Mater.* **2015**, *25*, 2166.
- [16] F. R. Fan, W. Tang, Z. L. Wang, *Adv. Mater.* **2016**, *28*, 4283.
- [17] H. Zou, Y. Zhang, L. Guo, P. Wang, X. He, G. Dai, H. Zheng, C. Chen, A. C. Wang, C. Xu, Z. L. Wang, *Nat. Commun.* **2019**, *10*, 1427.
- [18] G. Zhu, J. Chen, T. Zhang, Q. Jing, Z. L. Wang, *Nat. Commun.* **2014**, *5*, 3426.
- [19] S. Niu, Y. Liu, X. Chen, S. Wang, Y. S. Zhou, L. Lin, Y. Xie, Z. L. Wang, *Nano Energy* **2015**, *12*, 760.
- [20] E. M. Purcell, D. J. Morin, *Electricity and Magnetism*, Cambridge University Press, Cambridge, UK **2013**.
- [21] S. Niu, S. Wang, Y. Liu, Y. S. Zhou, L. Lin, Y. Hu, K. C. Pradel, Z. L. Wang, *Energy Environ. Sci.* **2014**, *7*, 2339.
- [22] Y. S. Zhou, G. Zhu, S. Niu, Y. Liu, P. Bai, Q. Jing, Z. L. Wang, *Adv. Mater.* **2014**, *26*, 1719.
- [23] G. Box, *Technometrics* **1988**, *30*, 1.
- [24] K. E. Barbour, C. G. Helmick, K. A. Theis, L. B. Murphy, J. M. Hootman, T. J. Brady, Y. Cheng, *Morb. Mortal. Wkly. Rep.* **2013**, *62*, 869.
- [25] G. Kwakkel, B. J. Kollen, H. I. Krebs, *Neurorehabil. Neural Repair* **2008**, *22*, 111.
- [26] D. Knudson, *Fundamentals of Biomechanics*, Springer Science & Business Media, New York **2007**.
- [27] H. Kazerooni, in *2005 IEEE/RSJ Int. Conf. on Intelligent Robots and Systems*, IEEE, Piscataway, NJ, USA **2005**, pp. 3459–3464.